Coexistence of ferroelectricity and antiferroelectricity in 2D van der Waals multiferroic

Bo Peng

bo_peng@uestc.edu.cn

University of Electronic Science and Technology of China   https://orcid.org/0000-0001-9411-716X

Yangliu Wu
1450683589@qq.com

Haipeng Lu
University of Electronic Science and Technology of China

Xiaocang Han
Peking University

Chendi Yang
Laboratory of Advanced Materials, Department of Materials Science and Shanghai Key Lab of Molecular Catalysis and Innovative Materials, Fudan University

Nanshu Liu
Renmin University of China

Xiaoxu Zhao
Peking University   https://orcid.org/0000-0001-9746-3770

Liang Qiao
School of Physics, University of Electronic Science and Technology of China   https://orcid.org/0000-0003-2400-2986

Wei Ji
Renmin University of China   https://orcid.org/0000-0001-5249-6624

Renchao Che
Fudan University   https://orcid.org/0000-0002-6583-7114

Longjiang Deng
University of Electronic Science and Technology of China   https://orcid.org/0000-0002-8137-6151

Article

Keywords:

Additional Declarations: There is **NO** Competing Interest.

Coexistence of ferroelectricity and antiferroelectricity in 2D van der Waals multiferroic

Yangliu Wu[1], Haipeng Lu[1], Xiaocang Han[2], Chendi Yang[3], Nanshu Liu[5], Xiaoxu Zhao[2], Liang Qiao[4], Wei Ji[5], Renchao Che[3], Longjiang Deng[1]* and Bo Peng[1]*

[1]National Engineering Research Center of Electromagnetic Radiation Control Materials, School of Electronic Science and Engineering, University of Electronic Science and Technology of China, Chengdu 611731, China

[2]School of Materials Science and Engineering, Peking University, Beijing 100871, China

[3]Laboratory of Advanced Materials, Department of Materials Science, Collaborative Innovation Center of Chemistry for Energy Materials(iChEM), Fudan University, Shanghai 200433, China

[4]School of Physics, University of Electronic Science and Technology of China, Chengdu 611731, China

[5]Beijing Key Laboratory of Optoelectronic Functional Materials & Micro-Nano Devices, Department of Physics, Renmin University of China, Beijing 100872, China

*To whom correspondence should be addressed. Email address: bo_peng@uestc.edu.cn; denglj@uestc.edu.cn

Abstract

Multiferroic materials with a coexistence of ferroelectric and magnetic order have been intensively pursued to achieve the mutual control of electric and magnetic properties toward energy-efficient memory and logic devices. The breakthrough progress of 2D van der Waals magnet and ferroelectric encourages the exploration of low dimensional multiferroics, which holds the promise to understand inscrutable magnetoelectric coupling and invent advanced spintronic devices. However, confirming ferroelectricity with optical techniques is challenging on 2D materials, particularly in conjunction with antiferromagnetic orders in a single-layer multiferroic. The prerequisite of ferroelectric is the electrically switchable spontaneous electric polarizations, which must be proven through reliable and direct electrical measurements. Here we report the discovery of 2D vdW multiferroic with out-of-plane ferroelectric polarization in trilayer NiI_2 device, as revealed by scanning reflective magnetic circular dichroism microscopy and ferroelectric hysteresis loop. The evolutions of between ferroelectric and antiferroelectric phase have been unambiguously observed. Moreover, the magnetoelectric interaction is directly probed by external electromagnetic field control of the multiferroic domains switching. This work opens up opportunities for exploring new multiferroic orders and multiferroic physics at the limit of single or few atomic layers, and for creating advanced magnetoelectronic devices.

Multiferroic materials with a coexistence of ferroelectric and magnetic orders has been diligently sought after for a long time to achieve the mutual control of electric and magnetic properties toward the energy-efficient memory and logic devices[1-3]. But the two contrasting order parameters tend to be mutually exclusive in a single material[4]. Nondisplacive mechanisms introduce a paradigm for constructing multiferroics beyond the traditional limits of mutual obstruction of the ferroelectric and magnetic orders[5,6]. To date, the type I multiferroic $BiFeO_3$ is the only known room-temperature single-phase multiferroic material. Alternatively, the helical magnetic orders break the spatial inversion symmetry and simultaneously lead to electric orders[7,8], giving rise to type-II multiferroics. The quest for a new single-phase multiferroic remains an open challenge.

The emergence of 2D vdW magnets and ferroelectrics has opened new avenues for exploring low-dimensional physics on magnetoelectric coupling[9,10]. Diverse isolated vdW ferromagnets[11-13] and ferroelectrics[14,15] have enabled tantalizing opportunities to create 2D vdW spintronic devices with unprecedented performances at the limit of single or few atomic layers. Few of bulk crystals of transition-metal dihalides with a trigonal layered structure have been shown that the helical spin textures break inversion symmetries and induce an orthogonal ferroelectric polarization [16,17], but and definitive multiferroicity remains elusive at the limit of few atomic layers.

A recent work shows the possibility of discovery of type-II monolayer NiI_2 multiferroics using the optical measurements of second-harmonic-generation (SHG) and linear dichroism (LD)[18]. Our work has pointed that all-optical characterizations are not sufficient to make a judgement of a few- and single-layer multiferroic at the presence of non-collinear and antiferromagnetic orders[19]. The observed SHG and LD signals in few-layer NiI_2 originate from the magnetic-order-induced breaking of spatial-inversion[19,20]. The prerequisite of ferroelectric polarization is the non-vanishing spontaneous electric polarizations, which must be proven through reliable and direct electrical measurements, such as polarization- and current-electric field (*P-E* and *I-E*) hysteresis loops. To date, 2D vdW multiferroic has not been directly uncovered at the limit of few layers. Here, we report fascinating vdW multiferroic with coexistence of ferroelectricity and antiferroelectricity in few layer NiI_2 based on magneto-optical-electric joint-measurements. In this 2D vdW multiferroics, an unprecedented magnetic control of switching dynamics of ferroelectric domain has been observed.

Non-collinear antiferromagnetism in trilayer NiI_2

Due to the high reactivity of NiI_2 flakes, NiI_2 exfoliation and encapsulation by graphene and hexagonal boron nitride (hBN) flakes were carried out in a glove box (Fig. 1a and Supplementary Fig. 1). NiI_2 crystal shows rhombohedral structure with a repeating stack of three (I-Ni-I) layers, where Ni and I ions form a triangular lattice in each layer (Fig. 1b). The rhombohedral stacking has been atomically identified (Fig. 1c). The atom

arrangements of rhombohedral phase demonstrate signature hexagon-shaped periodic bright spots with equal contrast, validating the overlapping stack of I and Ni atoms along the c axis. The ADF-STEM and fast Fourier transform (FFT) show an interplanar spacing of 1.9 Å, consistent with the (110) lattice plane of rhombohedral NiI_2 crystal. Circularly polarized Raman spectra in the parallel (σ+/σ+ and σ-/σ-) configuration show only two distinct peaks in the NiI_2 device (Fig. 1d). The peak at ~124.7 cm^{-1} is assigned to the A_g phonon modes[22], and this polarization behavior is consistent with Raman tensor analysis for the rhombohedral structure of NiI_2[23]. The Raman feature at ~20 cm^{-1} is assigned to the interlayer shear mode (SM), which suggests that the NiI_2 is trilayer[20].

For optimal optical response and sensitivity to probe the magnetic properties, the photon energy should be chosen near the absorption edge[11,24]. Therefore, we first studied white-light magnetic circular dichroism (MCD) spectra of a trilayer NiI_2 device as a function of magnetic field perpendicular to the sample plane at 10 K (see Methods for details)[25]. There is a strong peak near 2.3 eV along with two weak features around 1.85 eV and 1.6 eV (Fig. 1e). By means of ligand-field theory, the peaks are attributed to the absorption transitions of p-d exciton states[26]. A pair of opposite MCD peaks with magnetic field manifestly appears at 2.3 eV, suggesting strong magneto-optical resonance. When the magnetic field is switched, MCD features is consistently reversed, and zero remanent MCD signal at ~2.3 eV is distinctly observed at 0 T, indicating antiferromagnetic orders at 10 K.

To further validate the magnetic order, the scanning RMCD microscope was used to image and measure the magnetic domains of the as-exfoliated trilayer NiI_2. The polar RMCD imaging is a reliable and powerful tool to unveil the 2D magnetism in the micro scale, and the RMCD intensity is proportional to the out-of-plane magnetization [24]. All magneto-optical measurements were carried out using a 2.33 eV laser with optimal detection sensitivity (see Methods for details). Figure 2a shows RMCD maps of a trilayer NiI_2 sweeping between -0.75 T and +0.75 T at 10 K. Remarkably, many micrometer-sized bimeron-like domains are observed in trilayer and another few-layer NiI_2 across the entire range of sweeping magnetic field[27]. The spin-up and spin-down domains exist in pairs (Fig. 2a and Supplementary Fig. 2). One typical bimeron-like domains in trilayer NiI_2 at 0 T and 10 K are shown in Fig. 2b. The RMCD signals in each bimeron-like domain display opposite sign and nearly equal intensities. The magnetic moments point upwards or downwards in the core region and gradually decrease away from the core, and approaches zero near the perimeter (Fig. 2c). This magnetic moment distribution possibly indicates a pair of topological spin meron and antimeron with opposite chirality in a cycloid ground state[28,29]. The bimeron-like magnetization textures remain robust in all magnetic field, indicating the bimeron-like domains are robust. The high stability of the bimeron-like magnetic domains probably

originate from the topological protection, which also contributes to the preservation of magnetization even if upon a reversal magnetic field of 0.75 T. The formation of bimeron-like magnetic domains may be related to the localized stress at the interface. But further deep studies must be done to reveal the exact physical mechanism.

Fig. 2d shows the RMCD loops of the trilayer NiI_2 sweeping between +3 T and -3 T at 10 K. The RMCD loops show a highly nonlinear behavior with magnetic field and plateau behaviors for the out-of-plane magnetization. The RMCD intensity near 0 T is suppressed and approaches zero, suggesting the vanishing remnant magnetization, which indicates a compensation of the out-of-plane magnetization and non-collinear AFM orders in the trilayer NiI_2[30]. And the gradual increases of the RMCD signal are observed with increasing magnetic field between ±1.2 and ±2.6 T, suggesting a spin-flop process. The spin-flop behaviors of the magnetization curve imply that the interlayer antiferromagnetic coupling of the non-collinear spins is complicated. Similar magnetic hysteresis loops have been demonstrated in another few-layer NiI_2, which show definite non-collinear AFM orders in the few-layer NiI_2 (Supplementary Fig. 2b).

Ferroelectricity in trilayer NiI_2 device

To determine ferroelectricity in few-layer NiI_2 device, we performed the frequency-dependent measurement of electric polarization via *I-E* and *P-E* hysteresis loops, which allows an accurate estimation of the electric polarization. We fabricated two heterostructure devices of graphene/hBN/NiI_2/graphene/hBN (Fig. 1a and Supplementary Fig. 1). The hBN flake was used as an excellent insulating layer to prevent large leakage current and guarantee the detections of ferroelectric (FE) features[31,32] (Supplementary Fig. 3). The hBN insulator shows a linear *P-E* behavior and a rectangle-shaped *I-E* loops (Supplementary Fig. 4), indicating excellent insulativity for ferroelectric hysteresis measurements (see Methods for details)[33,34]. The frequency-dependent *I-E* and *P-E* loops at 10 K are shown in Fig. 3, and the forward and backward scans of the electric polarization as a function of electric field show characteristic ferroelectric *I-E* and *P-E* hysteresis. Strikingly, a characteristic double-hysteresis loop of antiferroelectric (AFE) polarization emerges accompanied with decreasing remanent polarization (P_r). More importantly, a pair of opposite single peaks of switching current (*I*) are observed when sweeping voltage at 6.7 Hz, which is attribute to charge displacement and implies two stable states with inverse polarity (Fig. 3b and c). Whereas two pair of opposite bimodal peaks are observed when sweeping voltage at 1.3 Hz, which is attribute to AFE-FE and FE-AFE transitions under electric field sweeping (Fig. 3c)[35]. This suggests an evolution from FE to AFE polarization with frequency is observed[36,37], exhibiting the decisive evidence for coexistence of ferroelectric and antiferroelectric[38,39]. This comprehensive frequency-dependent evolution behaviors also confirm the coexistence of FE and AFE in another a few layers

NiI$_2$ (Supplementary Fig. 5).

The type-II multiferroicity has been demonstrated in the bulk NiI$_2$. However, the multiferroic identification for few-layer NiI$_2$ remains challenging and elusive. All-optical methods are unreliable to make a judgement of a few- and single-layer multiferroic at the presence of non-collinear and antiferromagnetic orders[19]. The bulk NiI$_2$ displays a helimagnetic state below critical temperature[16,17]. From symmetry considerations and a Ginzburg-Landau perspective[40,41], the helimagnetic state allows for the emergence of a ferroelectric polarization associated to the form:

$$\mathbf{P} = \gamma \mathbf{e} \times \mathbf{q} \qquad (1)$$

where $\mathbf{P}$ is the electric polarization, $\mathbf{e}$ is the spin rotation axis, $\mathbf{q}$ is the spin propagation vector of the spin spiral, and γ is a scalar parameter dependence with spin-orbit coupling. For monolayer NiI$_2$, the helimagnetic order can be modeled with a 7a×a supercell and an in-plane (x-y plane) spin cycloid, and the spin propagation vector $\mathbf{q}$ is displayed along the [210] direction (in lattice vector units)[42], as shown in in Fig. 3d. Thus, the in-plane (x-y plane) spin cycloid induces the in-plane electric polarization along the [010] direction (Fig. 3d). Actually, theoretical calculations have determined that the $\mathbf{q}$-vector in multi-layer and bulk NiI$_2$ is a consequence of the competition between magnetic exchange interactions between magnetic atoms[42,43]. In particular, intralayer ferromagnetic first-neighbor, intralayer antiferromagnetic third neighbor, and interlayer antiferromagnetic second-neighbor magnetic exchange interactions are the most relevant. In the monolayer limit, there are no interlayer interactions, hence the $\mathbf{q}$-vector is in-plane and determined by the competition between intralayer exchange interactions. For a trilayer NiI$_2$, the $\mathbf{q}$-vector is modulated not only by intralayer exchange interactions but also by interlayer exchange interactions. Assuming that interlayer exchange interactions cause the tilting out-of-plane cycloidal spin configuration from in-plane (x-y plane) configuration (Fig. 3d), the $\mathbf{e}$-vector is no longer parallel to the z-axis, leading to an out-of-plane ferroelectric polarization component. Figure 3e illustrates the extreme case where the in-plane (x-y plane) cycloidal configuration tilts to x-z plane, resulting in an out-of-plane ferroelectric polarization. This scenario suggests the observed out-of-plane ferroelectric polarization in the trilayer NiI$_2$ device, but the precise mechanism remains to be further studied in the future. In particular, equation (1) shows that two spin spiral configurations with $\mathbf{q}_1 = \mathbf{q}$ and $\mathbf{q}_2 = -\mathbf{q}$ will give rise to opposite electric polarizations $\mathbf{P} = -\mathbf{P}$. The first principles calculations in spin configuration with both $\mathbf{q}$ and $-\mathbf{q}$ are energetically equivalent, and therefore show same energies with and without spin-orbit coupling[42]. Thus, the emergence of opposite electric dipoles can be directly observed in the total electronic density of the system. The energy of spin cycloidal configurations with positive and negative $\mathbf{q}$-vectors (positive and negative ferroelectric polarization $\mathbf{P}$) is degenerate, which approve the coexistence of ferroelectric and antiferroelectric (Fig. 3f), consistent with the observed

coexistence of ferroelectric and antiferroelectric in trilayer NiI_2.

Magnetic control of ferroelectricity

To reveal the magnetoelectric coupling effect, we studied the magnetic control of ferroelectric properties in the trilayer NiI_2 device, as shown in Fig. 4. The P_r extracted from the *P-E* hysteresis loop is plotted as a function of out-of-plane magnetic field at different frequencies (Fig. 4a-c). The magnetic field causes a decrease in residual polarization at different frequencies (Fig. 4a-c and Supplementary Fig. 6), and the magnetic control of P_r shows frequency dependence of applied electric field (Fig. 4d). The magnetic control ratio reaches to ~7% by detuning the frequency (24.5 Hz) at 7 T, which is remarkable feature of multiferroic. To better understand the magnetic control behavior, we briefly discuss the possible mechanism that leads to the decrease in P_r caused by the magnetic field from a microscopic perspective. We only discuss ferroelectric polarization flops in the model of spiral magnets[40]. In zero fields spins rotate in the easy x-z plane, so that the spin rotation axis **e** is parallel to the y axis, and for **q** // x-y plane, **P** // z (Supplementary Fig. 7a and 7b). However, magnetic field in the z direction favors the rotation of spins in the x-y plane (Supplementary Fig. 7c and 7d), so that the spin rotation axis **e** is parallel to the z axis, in which case, **P** // x-y plane[40]. In short, applying a magnetic field parallel to the z-axis causes the spin rotation plane to tilt from the x-z plane to the x-y plane, and the corresponding ferroelectric polarization flops from the out-of-plane direction to the in-plane direction. Therefore, an out-of-plane magnetic field leads to a decrease of ferroelectric polarization in the out-of-plane direction, which is consistent with the observed decrease in P_r with increasing magnetic field. Furthermore, the decrease in the current peak accompanied by an increase in the coercive electric field due to the increased magnetic field is unambiguously observed (Fig. 4e and Supplementary Fig. 8). This is because the out-of-plane magnetic field causes the spin rotation plane to tilt from the x-z plane to the x-y plane, and the corresponding easy axis of ferroelectric polarization flops from the out-of-plane direction to the in-plane direction. The shifts of current peaks induced by ferroelectric switching vary with the magnetic field, but the background current remains constant, excluding the magnetoresistance effects (Fig. 4e and Supplementary Fig. 8). Finally, the switching time of ferroelectric domain under different magnetic fields at 10 K is calculated by KAI model[44] (Fig. 4f and 4g; Part A and B). The switching time τ increase as magnetic field increase, which signifies an even symmetry with magnetic field (Fig. 4h), consistent with the above mechanisms. At 10 K, the switching time τ, leading to a maximum enhancement of switching time by 20% (-7 T). This observation of robust control of ferroelectric properties by magnetic field, pointing to the potential use of few-layer NiI_2 as a research platform for studying the magneto-electric coupling physics in the two-dimensional limit and for fabricating advanced nano-

magnetoelectric devices.

In summary, we report a 2D vdW single-phase multiferroic NiI$_2$ few-layer crystal. We observed strong evidences for the coexistence of ferroelectric and non-collinear antiferromagnetism order via RMCD, *P-E* and *I-E* hysteresis loop. hysteresis loop. We achieve unprecedented magnetic control of ferroelectric properties in the NiI$_2$ trilayer. We envision that the 2D vdW single-phase multiferroic NiI$_2$ will provide numerous opportunities for exploring fundamental low-dimensional physics, and will introduce a paradigm shift for engineering new ultra-compact magnetoelectric devices.

Methods

Sample fabrication

NiI$_2$ flakes were mechanically exfoliated from bulk crystals via PDMS films in a glovebox, which were synthesized by chemical vapor transport method from elemental precursors with molar ratio Ni:I = 1:2. All exfoliated hBN, NiI$_2$ and graphene flakes were transferred onto pre-patterned Au electrodes on SiO$_2$/Si substrates one by one to create heterostructure in glovebox, which were further in-situ loaded into a microscopy optical cryostat for magneto-optical-electric joint-measurement. The whole process of NiI$_2$ sample fabrications and magneto-optical-electric measurements were kept out of atmosphere.

Magneto-optical-electric joint-measurement

The polar RMCD, white-light MCD, Raman measurements and ferroelectric *P-E* and *I-E* measurements were performed on a powerful magneto-optical-electric joint-measurement scanning imaging system (MOEJSI)[19], with a spatial resolution reaching diffraction limit. The MOEJSI system was built based on a Witec Alpha 300R Plus low-wavenumber confocal Raman microscope, integrated with a closed cycle superconducting magnet (7 T) with a room temperature bore and a closed cycle cryogen-free microscopy optical cryostat (10 K) with a specially designed snout sample mount and electronic transport measurement assemblies.

The Raman signals were recorded by the Witec Alpha 300R Plus low-wavenumber confocal Raman microscope system, including a spectrometer (150, 600 and 1800/mm) and a TE-cooling Andor CCD. A 532 nm laser of ~0.2 mW is parallel to the X-axis (0$^{\mathrm{o}}$) and focused onto samples by a long working distance 50× objective (NA = 0.55, Zeiss) after passing through a quarter-wave plate (1/4λ). The circular polarization resolved Raman signals passed through the same 1/4λ waveplate and a linear polarizer, obtained by the spectrometer (1800/mm) and the CCD.

For white-light MCD measurements, white light with Köhler illumination from Witec Alpha 300R Plus microscope was linearly polarized at 0o by a visible wire grid

polarizer, passed through an achromatic quarter-wave ($1/4\lambda$) plate and focused onto samples by a long working distance 50× objective (Zeiss, NA = 0.55). The right-handed and left-handed circularly polarized white light was obtained by rotating $1/4\lambda$ waveplate at +45° and -45°. The white-light spectra were recorded by the Witec Alpha 300R Plus confocal Raman microscope system (spectrometer, 150/mm). The absorption spectra of right-handed and left-handed circularly polarized light in different magnetic field can be obtained as the previous work[25], giving corresponding MCD spectra.

For polar RMCD measurements, a free-space 532 nm laser (2.33 eV) of ~2 μW modulated by photoelastic modulator (PEM, 50 KHz) was reflected by a non-polarizing beamsplitter cube (R/T = 30/70) and then directly focused onto samples by a long working distance 50× objective (NA = 0.55, Zeiss), with a diffraction limit spatial resolution of ~590 nm. The reflected beam which was collected by the same objective passed through the same non-polarizing beamsplitter cube and was detected by a photomultiplier (PMT), which was coupled with lock-in amplifier, Witec scanning imaging system, superconducting magnet, voltage source meter and ferroelectric tester. Ferroelectric *P-E* and *I-E* hysteresis loop of a NiI_2 device of $Gr/hBN/NiI_2/Gr$ were measured by classical ferroelectric measurements and directly recorded by ferroelectric tester (Precision Premier II: Hysteresis measurement), which were contacted with the top and bottom graphene electrodes by patterned Au electrodes (Fig. 1a) through the electronic assemblies of the microscopy optical cryostat. The mechanism of ferroelectric measurement has been given by previous work[45]. The detected signals include two components: a ferroelectric term of NiI_2 (2PrA) and a linear non-ferroelectric term of hBN insulator (σEAt), Q = QNiI + QBN = 2PrA + σEAt. If only hBN insulator, a linear P-E loop take place, consistent with our experimental results of hBN flake (Supplementary Fig. 4). The linear hBN background have no effect on the ferroelectric features, and hBN flakes as excellent insulator suppress and overcome the leakage current, which for guarantee the detections of NiI_2 ferroelectric features[31-34].

STEM Imaging, Processing, and Simulation
Atomic-resolution ADF-STEM imaging was performed on an aberration-corrected JEOL ARM 200F microscope equipped with a cold field-emission gun operating at 80 kV. The convergence semiangle of the probe was around 30 mrad. Image simulations were performed with the Prismatic package, assuming an aberration-free probe with a probe size of approximately 1 Å. The convergence semiangle and accelerating voltage were in line with the experiments. The collection angle for ADF imaging was between 81 and 228 mrad. ADF-STEM images were filtered by Gaussian filters, and the positions of atomic columns were located by finding the local maxima of the filtered series.

Data availability

The data that support the findings of this study are available from the corresponding authors upon reasonable request. Source data are provided with this paper.

References

1   Fiebig, M., Lottermoser, T., Meier, D. & Trassin, M. The evolution of multiferroics. *Nat. Rev. Mater.* **1**, 16046, (2016).

2   Chu, Y.-H. et al. Electric-field control of local ferromagnetism using a magnetoelectric multiferroic. *Nat. Mater.* **7**, 478-482, (2008).

3   Ponet, L. et al. Topologically protected magnetoelectric switching in a multiferroic. *Nature* **607**, 81-85, (2022).

4   Cheong, S.-W. & Mostovoy, M. Multiferroics: a magnetic twist for ferroelectricity. *Nat. Mater.* **6**, 13-20, (2007).

5   Wang, J. et al. Epitaxial $BiFeO_3$ multiferroic thin film heterostructures. *Science* **299**, 1719-1722, (2003).

6   Guo, R. et al. Continuously controllable photoconductance in freestanding $BiFeO_3$ by the macroscopic flexoelectric effect. *Nat. Commun*. **11**, 2571, (2020).

7   Kimura, T. et al. Magnetic control of ferroelectric polarization. *Nature* **426**, 55-58, (2003).

8   Hur, N. et al. Electric polarization reversal and memory in a multiferroic material induced by magnetic fields. *Nature* **429**, 392-395, (2004).

9   Rogée, L. et al. Ferroelectricity in untwisted heterobilayers of transition metal dichalcogenides. *Science* **376**, 973-978, (2022).

10 Yang, Q. et al. Ferroelectricity in layered bismuth oxide down to 1 nanometer. *Science* **379**, 1218-1224, (2023).

11 Huang, B. et al. Layer-dependent ferromagnetism in a van der Waals crystal down to the monolayer limit. *Nature* **546**, 270-273, (2017).

12 Gong, C. et al. Discovery of intrinsic ferromagnetism in two-dimensional van der Waals crystals. *Nature* **546**, 265–269, (2017).

13 Deng, Y. et al. Gate-tunable room-temperature ferromagnetism in two-dimensional Fe_3GeTe_2. *Nature* **563**, 94-99, (2018).

14 Yuan, S. et al. Room-temperature ferroelectricity in $MoTe_2$ down to the atomic monolayer limit. *Nat. Commun*. **10**, 1775, (2019).

15 Liu, F. et al. Room-temperature ferroelectricity in $CuInP_2S_6$ ultrathin flakes. *Nat. Commun.* **7**, 12357, (2016).

16 Kurumaji, T. et al. Magnetoelectric responses induced by domain rearrangement and spin structural change in triangular-lattice helimagnets NiI_2 and CoI_2. *Phys. Rev. B*

87, 014429, (2013).

17   Zhao, L. et al. CuBr$_2$ – a new multiferroic material with high critical temperature. *Adv. Mater.* **24**, 2469-2473, (2012).

18   Song, Q. et al. Evidence for a single-layer van der Waals multiferroic. *Nature* 602, 601-605, (2022).

19   Jiang, Y. et al. Dilemma in optical identification of single-layer multiferroics. *Nature* **619**, E40-E43, (2023).

20   Wu, S. et al. Layer thickness crossover of type-II multiferroic magnetism in NiI$_2$. arXiv:2307.10686 (2023).

21   Sun, Z. et al. Giant nonreciprocal second-harmonic generation from antiferromagnetic bilayer CrI$_3$. *Nature* **572**, 497-501, (2019).

22   Liu, H. et al. Vapor deposition of magnetic van der Waals NiI$_2$ crystals. *ACS Nano* **14**, 10544-10551, (2020).

23   Guo, K. et al. Layer dependence of stacking order in nonencapsulated few-layer CrI$_3$. *Sci. China. Mater.* **63**, 413-420, (2020).

24   Wang, X. et al. Light-induced ferromagnetism in moiré superlattices. *Nature* **604**, 468-473, (2022).

25   Mak, K. F. et al. Measurement of the optical conductivity of graphene. *Phys. Rev. Lett.* **101**, 196405 (2008).

26   Pollini, I., Thomas, J. & Lenselink, A. Optical properties of layered transition-metal iodides. *Phys. Rev. B* **30**, 2140-2148, (1984).

27   Wu, X. et al. Topology-induced chiral photon emission from a large-scale meron lattice. *Nat. Electron.* **6**, 516-524, (2023).

28   Wintz, S. et al. Topology and origin of effective spin meron pairs in ferromagnetic multilayer elements. *Phys. Rev. Lett.* **110**, 177201, (2013).

29   Xu, C. et al. Electric-field switching of magnetic topological charge in type-I multiferroics. *Phys. Rev. Lett.* **125**, 037203, (2020).

30   Xie, H. et al. Evidence of non-collinear spin texture in magnetic moiré superlattices. *Nature Physics* **19**, 1150-1155, (2023).

31   Knobloch, T. et al. The performance limits of hexagonal boron nitride as an insulator for scaled CMOS devices based on two-dimensional materials. *Nat. Electron.* **4**, 98-108, (2021).

32   Yang, T. H. et al. Ferroelectric transistors based on shear-transformation-mediated rhombohedral-stacked molybdenum disulfide. *Nat. Electron.* **7**, 29–38 (2024).

33   Park, J. Y. et al. Revival of Ferroelectric Memories Based on Emerging Fluorite-Structured Ferroelectrics. *Adv. Mater.* **35**, 2204904, (2023).

34   Kim, Y., Min, K. K., Yu, J., Kwon, D. & Park, B.-G. Lamination method for improved polarization-leakage current relation in HfO$_2$-based metal/ferroelectric/insulator/semiconductor structure. *Semicond. Sci. Technol.* **37**,

045001, (2022).

35   Wu, Z. et al. Discovery of an above-room-temperature antiferroelectric in two-dimensional hybrid perovskite. *J. Am. Chem. Soc*. **141**, 3812-3816, (2019).

36   Park, M. H. et al. Ferroelectricity and antiferroelectricity of doped thin HfO_2-based films. *Adv. Mater*. **27**, 1811-1831, (2015).

37   Müller, J. et al. Ferroelectricity in Simple Binary ZrO_2 and HfO_2. *Nano Lett.* **12**, 4318-4323, (2012).

38   Ko, K. et al. Operando electron microscopy investigation of polar domain dynamics in twisted van der Waals homobilayers. *Nat. Mater*. **22**, 992–998 (2023).

39   Xu, B., Paillard, C., Dkhil, B. & Bellaiche, L. Pinched hysteresis loop in defect-free ferroelectric materials. *Phys. Rev. B* **94**, 140101 (2016).

40   Mostovoy, M. Ferroelectricity in spiral magnets. *Phys. Rev. Lett.* **96**, 067601, (2006).

41   Hohenberg, P. C. et al. An introduction to the Ginzburg–Landau theory of phase transitions and nonequilibrium patterns *Phys. Rep*. **572**, 1–42, (2015).

42   Fumega, A. O. et al. Microscopic origin of multiferroic order in monolayer NiI_2. *2D Mater*. **9**, 025010, (2022).

43   Riedl, K. et al. Microscopic origin of magnetism in monolayer $3d$ transition metal dihalides. *Phys. Rev. B* **106**, 035156, (2022).

44   Zhao, D., Katsouras, I., Asadi, K., Blom, P. W. M. & de Leeuw, D. M. Switching dynamics in ferroelectric P(VDF-TrFE) thin films. *Phys. Rev. B* **92**, 214115, (2015).

45   Scott, J. F. et al. Ferroelectrics go bananas. *J. Phys.: Condens.Matter* **20**, 021001, (2008).

46   Golla, D. et al. Optical thickness determination of hexagonal boron nitride flakes. *Appl. Phys. Lett*. **102**, 161906, (2013).

Acknowledgments

Author contributions

B.P conceived the project. Y.W. prepared the samples and performed the magneto-optical-electric joint-measurements and Raman measurements assisted by B.P., and performed the ferroelectric measurements assisted by L.Q., and analyzed and interpreted the results assisted by H.L., N. L., W.J., L.D. and B.P.. C. Y, R.C, X.X. and X.H. performed the STEM measurements. Y.W. and B.P. wrote the paper with input from all authors. All authors discussed the results.

## Competing interests

The authors declare no competing interests.

Additional information

**Supplementary information** is available for this paper at xxx (will be provided).

Correspondence and requests for materials should be addressed to B.P.

Reprints and permission information is available online at http://www.nature.com/reprints.

Publisher's note Springer Nature remains neutral with regard to jurisdictional claims in published maps and institutional affiliations.
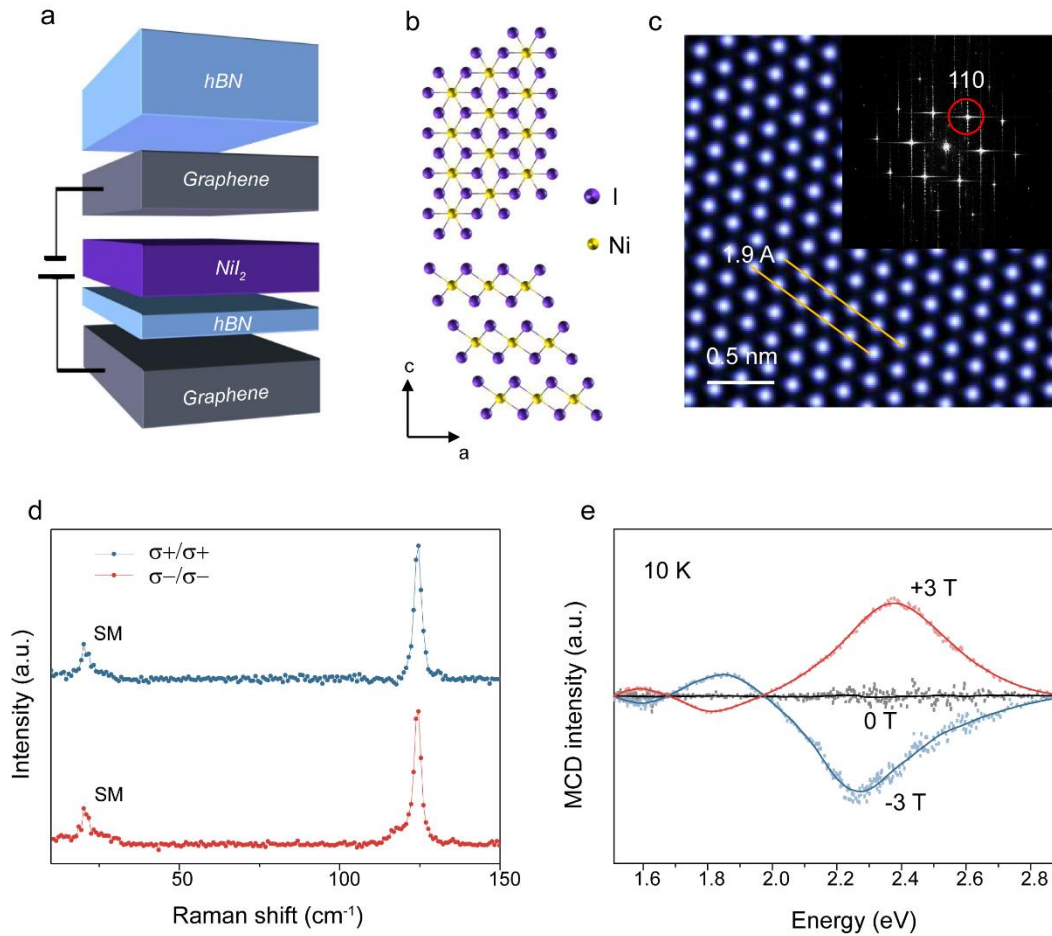
**Fig. 1 | Crystal structure, MCD measurements of trilayer NiI₂ at room temperature. a,** Schematic of trilayer NiI_2 sandwiched between graphene and hBN. **b,** View of the in-plane and out-of-plane atomic lattice. The magnetic Ni^{2+} ions are surrounded by the octahedron of I^- ions, and three NiI_2 layers as a repeating unit stack in a staggered fashion along the c axis. **c,** Atomic-resolution ADF-STEM image showing signature hexagonal patterns of rhombohedral stacking in few-layer NiI_2 crystals. The inset shows the corresponding FFT image. **d,** Circular polarization resolved Raman spectra of a trilayer NiI_2 device (Fig. 1a) at room temperature, excited by 532 nm laser. "SM" indicates the interlayer shear mode of trilayer NiI_2. **e,** The MCD spectra of trilayer NiI_2 at +3 T, 0 T and -3T. MCD signals are sensitive to spin electronic transitions and magnetic moments in the electronic states. The MCD features are spin-sign dependent and reverse as magnetic field switch. The zero remanent MCD signals at ~2.3 eV at 0 T suggest antiferromagnetic orders.
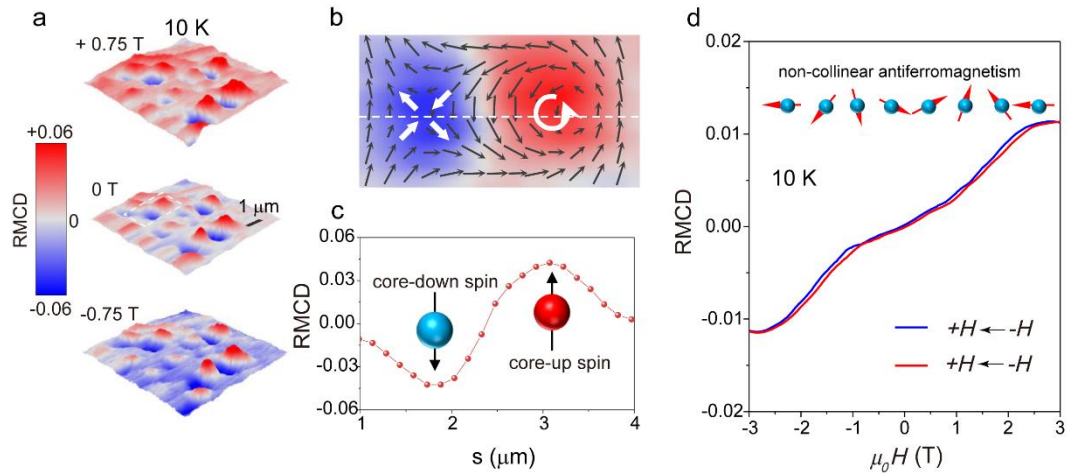
Fig. 2 | Non-collinear antiferromagnetism in trilayer NiI₂ device. a, Polar RMCD maps upon a 2.33 eV laser with diffraction-limited spatial resolution (see Methods), collected at room temperature and selected magnetic field. **b,** Schematic of the spin textures of bimerons-like domains and corresponding zoom-in RMCD images (white dashed-line box in Fig. 2a). **c,** The polar RMCD signals along with the line sections of RMCD map (**b**). **d,** The RMCD curves sweeping between +3 T and -3 T at 10 K, suggesting a non-collinear antiferromagnetism.
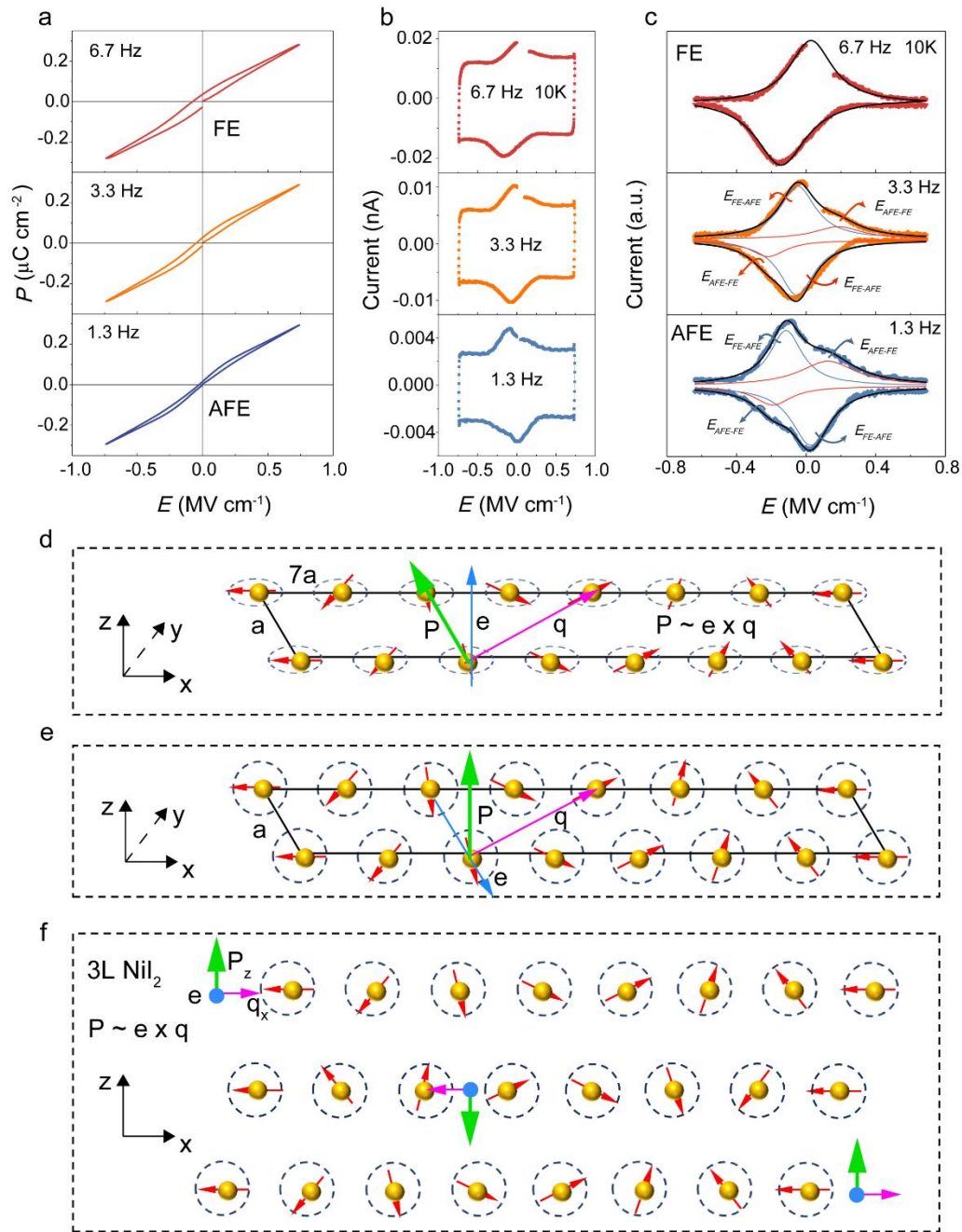
Fig. 3 | Existence of ferroelectric and anti-ferroelectric orders in trilayer NiI₂ device. a, b, *P-E* and *I-E* loops at various frequencies from device 1 (D1). **c,** Corresponding *I-E* loops from Fig. 3b subtracted the current background. Two pairs of current peaks (FE-AFE and AFE-FE switching peaks) were obtained by Lorentz fitting. An evolution from FE to AFE was observed. **d,** Schematic of the spin spiral configurations with in-plane (x-y plane) spin cycloid in monolayer NiI₂, showing a periodicity of 7×1 unit cells. **e,** Extreme case where the in-plane (x-y plane) cycloidal configuration tilts to x-z plane caused by interlayer exchange interactions, resulting in an out-of-plane ferroelectric polarization. **f,** Schematic of the spin spiral configurations with opposite **q** in trilayer NiI₂, showing the coexistence of ferroelectric and antiferroelectric.
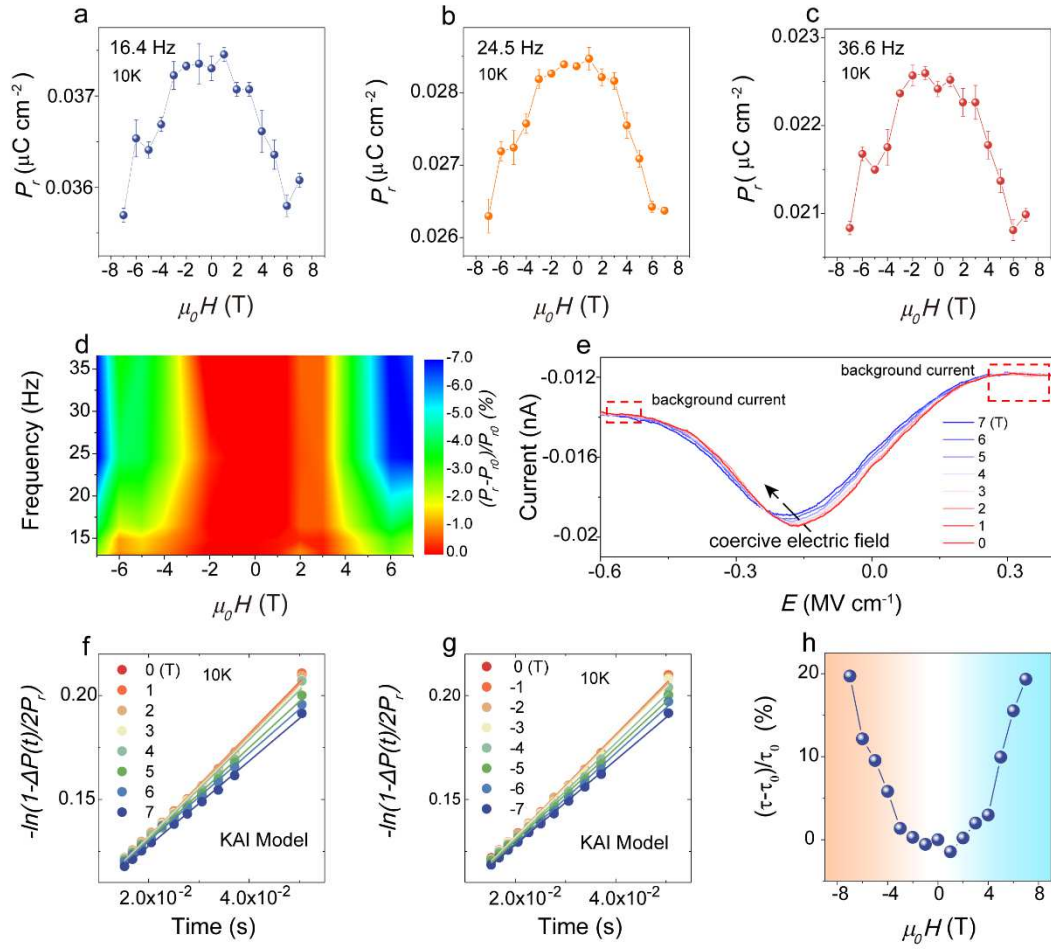
Fig. 4 | Magnetic control of ferroelectricity in trilayer NiI₂ device. a-c, The P_r extracted from the *P-E* hysteresis loop is plotted as a function of out-of-plane magnetic field at different frequencies. The error bars are standard deviations of P_r. **d,** The magnetic control ratio $(P_r - P_{r0})/P_{r0}$ are frequency dependent, where P_r and P_{r0} is remanent polarization in a magnetic field and without magnetic field, respectively. **e,** The *I-E* curves at different magnetic field. The decrease in the current peak accompanied by an increase in the coercive field due to the increased magnetic field is unambiguously observed. **f, g,** Fitting by KAI model for different magnetic field at 10 K, giving the switching time τ. **h,** The $(\tau-\tau_0)/\tau_0$ as a function of magnetic field at 10 K, indicating a degree of magnetic control of switching time, where τ and τ_0 is switching time in a magnetic field and without magnetic field, respectively.

Supplementary Files

This is a list of supplementary files associated with this preprint. Click to download.

- SI.pdf